




Cite this: *CrystEngComm*, 2024, 26, 4820

## Chemical catalytic degradation of organic pollutants by using Ag–Cu<sub>2</sub>O core–shell decorated on rGO†

Lei Chen,<sup>a</sup> Shuang Guo,<sup>b</sup> Eungyeong Park,<sup>c</sup> Hongkai Zhao<sup>\*a</sup> and Young Mee Jung <sup>\*bc</sup>

We successfully fabricated Ag@Cu<sub>2</sub>O core–shell decorated on reduced graphene oxide (rGO) nanocomposites (ACRN) with a simple and convenient *in situ* substitution method. The properties of these ACRNs with heterostructure layers were characterized by scanning and transmission electron microscopy and absorption spectroscopy. We used 4-nitrophenol (4-NP) as a probe molecule to determine the chemical catalytic activity of the ACRN. Upon introduction of rGO, a high electron transfer efficiency was achieved; thus, the catalytic activity was improved significantly. Therefore, the ACRN exhibited significantly improved catalytic activity for the reduction of 4-NP and showed high application value in the removal of toxic and harmful substances from water. The catalytic efficiency was improved by 1.7 times by using the ACRN compared to Ag–rGO. In addition, the fabricated ACRN was used for the reduction of an organic dye (methyl orange, MO), and explosive pollutant (trinitrophenol, TNP) to generate nontoxic products. Furthermore, the high charge redistribution and transfer among Ag, Cu<sub>2</sub>O, and rGO in the ACRN induced the high catalytic reduction of organic pollutants, indicating the excellent potential of these materials for applications in water pollution treatment.

Received 27th June 2024,  
Accepted 29th July 2024

DOI: 10.1039/d4ce00644e

[rsc.li/crystengcomm](http://rsc.li/crystengcomm)

### Introduction

As a result of industrial development, environmental pollution by nitro compounds in water has become increasingly serious and has received widespread attention from all sectors of society.<sup>1,2</sup> 4-Nitrophenol (4-NP) and other phenolic pollutants are the most representative pollutants in industrial wastewater.<sup>3,4</sup> They are carcinogenic and mutagenic and pose a considerable threat to the environment and human health.<sup>5,6</sup> Catalytic hydrogenation has the advantages of being simple and less polluting to the environment during the treatment of phenolic pollutant compounds. This method has potential development prospects. At present, the key to the catalytic hydrogenation process for treating nitrophenol compounds is to develop efficient, stable, and low-cost catalysts. Therefore, many kinds of inorganic catalysts have

been designed and fabricated for the catalysis of phenolic pollutants.<sup>7–10</sup>

Traditional catalysts, including noble metals (*e.g.*, Pt, Pd, Au, and Ag), were widely used in 4-NP catalytic hydrogenation.<sup>11–14</sup> These catalysts exhibit high catalytic activity under mild reaction conditions. Extensive studies on these types of catalysts have been conducted worldwide. However, the challenge is to develop new types of catalysts that are stable, highly active, and reusable. Therefore, metal/semiconductor composites have been developed. The interface of the metal/semiconductor heterojunctions has outstanding advantages in catalytic applications. Due to the strong interaction between metals and semiconductors at the interface, charge transfer (CT) and transfer between the components in the composite region are the main features that cause significant changes at the heterojunction interface. More importantly, the stability of the nanocomposite is better than that of the individual components. In addition, the catalytic properties can be easily controlled by changing the morphology, composition, and geometric structure of the material. Metal/semiconductor composites are excellent functional materials and are widely used in various materials.<sup>15–18</sup> In addition, core–shell nanostructures have been designed and fabricated to solve the problems of a single mechanism and limited material properties.<sup>19,20</sup> Therefore, Ag@Cu<sub>2</sub>O nanoparticles were used for the

<sup>a</sup> School of Materials Science and Engineering, Jilin Jianzhu University, Changchun 130118, China. E-mail: [hkzhao003@126.com](mailto:hkzhao003@126.com)

<sup>b</sup> Department of Chemistry, Institute for Molecular Science and Fusion Technology, Kangwon National University, Chuncheon 24341, Korea. E-mail: [ymjung@kangwon.ac.kr](mailto:ymjung@kangwon.ac.kr)

<sup>c</sup> Kangwon Radiation Convergence Research Support Center, Kangwon National University, Chuncheon 24341, Korea

† Electronic supplementary information (ESI) available. See DOI: <https://doi.org/10.1039/d4ce00644e>

chemical catalysis of phenolic pollutants. The difference in energy between Ag nanoparticles and  $\text{Cu}_2\text{O}$  induces electron transfer between the core and shell.<sup>21,22</sup>

Two-dimensional (2D) materials show extraordinary mechanical, optical, electronic, and thermal properties, which can expand their applications. Graphene, due to its high charge carrier mobility, has demonstrated excellent performance and has received extensive research attention since it was developed as a novel 2D material in 2004.<sup>23,24</sup> The mechanical and electronic properties of monolayer or multilayer 2D graphene have made it a hot research topic in nanoelectronics. Therefore, graphene has been widely used in different catalysis systems. Graphene is also widely used in batteries, supercapacitors, solar cells, detectors, and sensors due to its excellent performance.<sup>25,26</sup>  $\text{Ag}@Cu_2O$  core-shell decorated on reduced graphene oxide (rGO) nanocomposites (ACRNs) exhibited excellent catalytic activity because the  $\text{Cu}_2\text{O}$  shell was *in situ* growing on the Ag-rGO surface. After the introduction of rGO onto the  $\text{Ag}@Cu_2O$  core-shell, the material exhibited excellent catalytic performance and carrier transport.<sup>20</sup>

In this study, ACRNs were fabricated for catalytic studies. Ag-rGO nanocomposites were synthesized using the sol-gel method, and  $\text{Ag}@Cu_2O$  nanocomposites were obtained by reducing cupric nitrate ( $\text{Cu}(\text{NO}_3)_2$ ) in the presence of the hydrazine hydrate ( $\text{N}_2\text{H}_4$ ). By tuning the concentration of  $\text{Cu}(\text{NO}_3)_2$ , the thickness of the  $\text{Cu}_2\text{O}$  shell of  $\text{Ag}@Cu_2O$  can be controlled. These materials show different catalytic properties and are expected to solve water pollution problems. The increased number of available free electrons led to random adsorption of the ACRN by the catalytic target. More importantly, the ACRN showed high adsorption capacity, which greatly enhanced their catalytic activity for 4-NP, methyl orange (MO), and trinitrophenol (TNP).

## Results and discussion

### Morphological characterization of the ACRN

To obtain the ACRN, we first fabricated Ag decorated on rGO (Ag-rGO) using the wet chemical method (Fig. 1A). The Ag on rGO acted as a nucleation site for the  $\text{Cu}_2\text{O}$  shell coating. By decreasing the volume of the Ag-rGO composite solution, the density of the  $\text{Ag}@Cu_2O$  decorated on rGO was significantly increased. Meanwhile, the size of the  $\text{Ag}@Cu_2O$  spheres increased significantly with the increase of the  $\text{Cu}_2\text{O}$  shell thickness. Scanning electron microscope (SEM) images were obtained to characterize the morphology of the ACRN. As shown in Fig. S1,<sup>†</sup> after surface modification, the composite material maintained the 2D structure of rGO and spherical nanoparticles was arranged on the surface, indicating the successful fabrication of  $\text{Ag}@Cu_2O$  composites on the rGO platform. To confirm the core-shell structure, we obtained transmission electron microscope (TEM) images. As shown in Fig. 2, the composites (Fig. 2B–D) we fabricated possessed a clear Ag- $\text{Cu}_2\text{O}$  core-shell structure decorated on the rGO substrate. Fig. 2A shows Ag decorated on the rGO substrate,

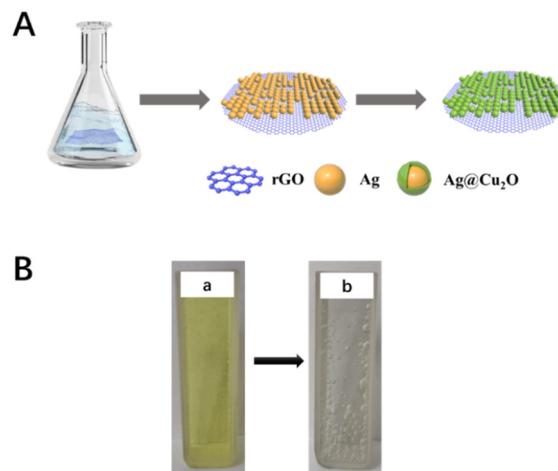


Fig. 1 (A) Schematic diagram of the ACRN preparation. (B) Optical photos of the reduction of 4-NP using the ACRN-2. (a) After the addition of  $\text{NaBH}_4$ , 4-NP was ionized and the color of solution changed to light yellow; (b) the decomposition of 4-NP was complete and the solution turned colorless.

and the average diameter of the Ag nanoparticles is 13 nm. By introducing 15 mL of Ag-rGO composite,  $\text{Cu}_2\text{O}$  was formed and covered the Ag core. However, the Ag core was not fully covered by the  $\text{Cu}_2\text{O}$  shell (ACRN-1, Fig. 2B), and the average diameter of the Ag- $\text{Cu}_2\text{O}$  nanocomposites was 22 nm. As the volume of the Ag-rGO composite decreased, the thickness of the  $\text{Cu}_2\text{O}$  shell increased significantly, which could completely cover the Ag core (ACRN-2 and ACRN-3, Fig. 2C and D), and the average diameter of the Ag- $\text{Cu}_2\text{O}$  core-shell were 27 (ACRN-2, the range of the diameters is 17–35 nm) and 30 nm (ACRN-3, the range of the diameters was 21–39 nm) shown in Fig. S2.<sup>†</sup> Comparative observation showed that as the amount of the Ag-rGO composite decreased, the shell thickness of  $\text{Cu}_2\text{O}$  also gradually increased until the thicknesses were approximately 14 (ACRN-2) and 17 nm (ACRN-3). Therefore, by controlling the

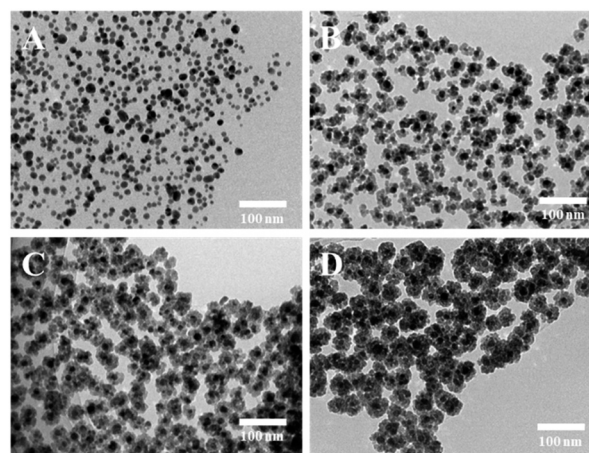


Fig. 2 TEM images of Ag-rGO (A) and ACRNs with different thicknesses of the  $\text{Cu}_2\text{O}$  shell (B–D). The thickness of the  $\text{Cu}_2\text{O}$  shell is about 9 (B), 14 (C), and 17 nm (D).

amount of the Ag-rGO composite and then controlling the thickness of the composite shell, composites with different structural properties were prepared. In the TEM images, we could observe that the surface of the Cu<sub>2</sub>O shell was rough and porous, which is conducive to molecular adsorption. The loose structure on the Cu<sub>2</sub>O surface increased the catalytic and active sites, which promoted catalytic reduction of the target.

The elemental composition of Ag-rGO and ACRNs with different thicknesses of the Cu<sub>2</sub>O shell was studied by the X-ray photoelectron spectroscopy (XPS) method. As shown in Fig. 3, we observed the XPS spectra of the Ag, C, O, and Cu elements of Ag-rGO and ACRNs with different thicknesses of the Cu<sub>2</sub>O shell.<sup>27,28</sup> In Fig. 3(A), the peaks of Ag 3d<sub>5/2</sub> and Ag 3d<sub>3/2</sub> were observed at 366.6 and 372.5 eV. With the increase of the thickness of the Cu<sub>2</sub>O shell, the peaks of Ag decreased significantly, which was attributed to the shielding effect of the Cu<sub>2</sub>O shell. The two main C 1s peaks at 284.6 and 287.1 eV, assigned to the C-C and C-O, are shown in Fig. 3(B). After coating with the Cu<sub>2</sub>O shell, we found that the C 1s peak at 287.1 eV was shifted to a lower energy, which is attributed to the CT between rGO and Cu<sub>2</sub>O. In Fig. 3(C), we observed the O 1s peaks at 529.0, 530.2, and 531.7 eV, corresponding to lattice oxygen, oxygen adsorbed from the Cu<sub>2</sub>O shell, and the C-O group from rGO, respectively. The Cu 2p<sub>3/2</sub> and Cu 2p<sub>1/2</sub> peaks assigned to the Cu<sub>2</sub>O shell appeared at 930.4 and 950.3 eV, as shown in Fig. 3(D). As the thickness of the Cu<sub>2</sub>O shell increased, the intensity of the Cu 2p<sub>3/2</sub> and Cu 2p<sub>1/2</sub> peaks increased significantly. Meanwhile, new shoulder peaks

appeared at high energy peaks around 930.4 and 950.3 eV, indicating partial oxidation of Cu<sub>2</sub>O.

To study the light response of the different ACRNs, we obtained the UV-vis spectra of different ACRNs (Fig. 4). The spectra of ACRNs with different shell thicknesses exhibited plasmon resonance absorption peaks. Comparative observation showed that the plasmon resonance absorption peak gradually weakened as the amount of Ag-rGO increased. The peaks at approximately 250–300 and 300–500 nm were assigned to the C=C and C=O bands of rGO, which were assigned to the surface plasmon resonance (SPR) of Ag decorated on rGO.<sup>29</sup> In addition, the peak at 500–700 nm corresponded to the SPR of the core-shell structure, and the optical absorbance increased significantly with increasing thickness of the Cu<sub>2</sub>O nanoshell. The slight redshift of the peak at 500–700 nm was attributed to the increase in the local dielectric constant of Cu<sub>2</sub>O.<sup>30</sup>

### Catalytic performance analysis

The harmful effects of organic pollutants have received widespread attention. Developing methods to catalytically degrade these pollutants is of great importance. 4-NP has been widely used in the synthesis of pesticides, drugs, and dyes, showing their potential hazards. Therefore, various catalytic materials have been designed and fabricated to reduce it.<sup>3,4</sup>

We used 4-NP as a probe molecule to evaluate the catalytic performance of the ACRN. The catalytic rate for 4-NP (0.005 M) was significantly increased by the addition of the ACRN. We observed the absorption peak of 4-NP at about 320 nm (Fig. 5A–D). After the addition of NaBH<sub>4</sub>, 4-NP was ionized, resulting in the red-shifted peak at about 400 nm (Fig. 5A–D), and the solution was changed to light yellow (Fig. 1B-a). After the complete degradation of 4-NP, the solution in the cuvette became colorless (Fig. 1B-b), mainly due to the formation of ionic 4-NP.

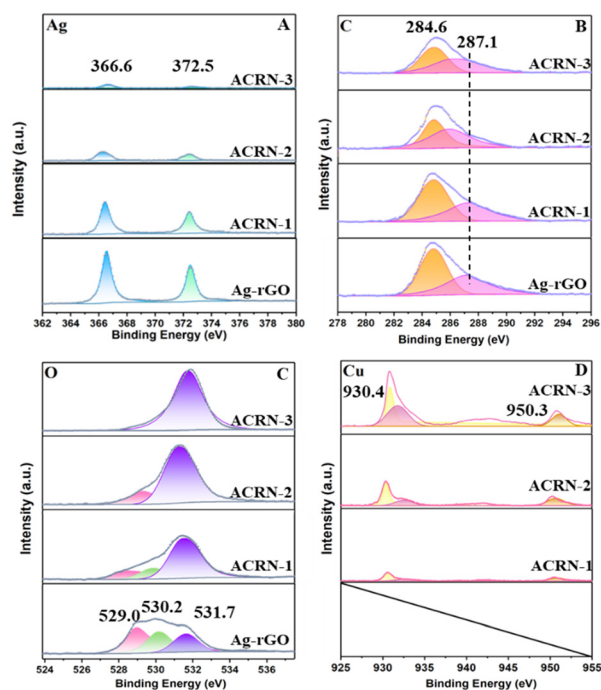


Fig. 3 XPS spectra of (A) Ag, (B) C, (C) O, and (D) Cu in Ag-rGO and ACRNs with different thicknesses of the Cu<sub>2</sub>O shell (ACRN-1, ACRN-2, and ACRN-3).

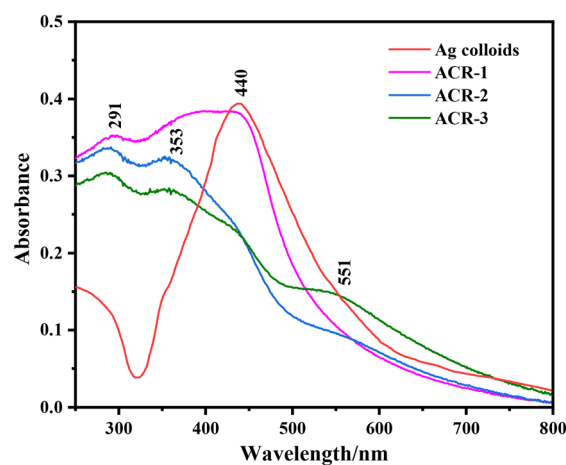


Fig. 4 UV-vis absorption spectra of Ag colloids and ACRNs with different thicknesses of the Cu<sub>2</sub>O shell. The thickness of the Cu<sub>2</sub>O shell is about 9 (ACRN-1), 14 (ACRN-2), and 17 nm (ACRN-3).

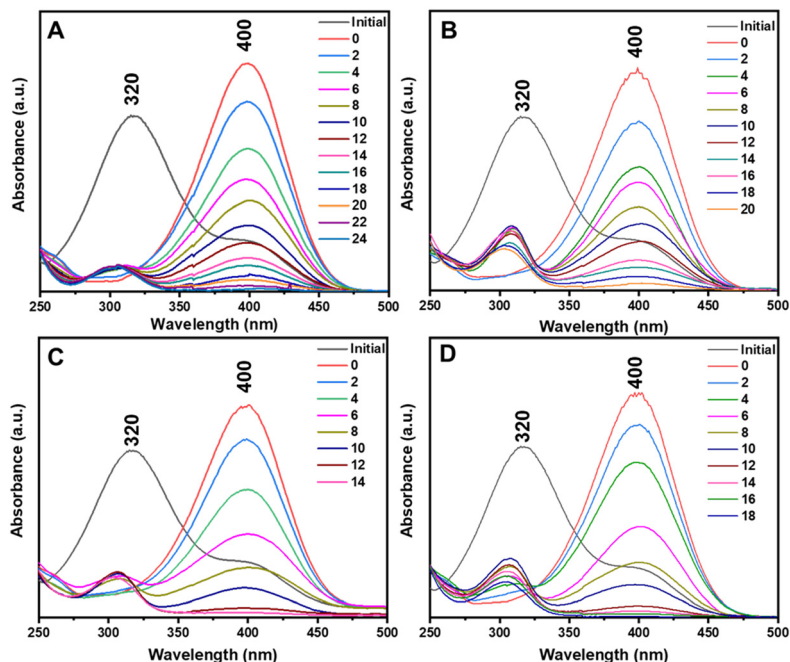


Fig. 5 UV-vis absorption spectra of the reduction of 4-NP by the introduction of (A) Ag-rGO ( $t = 24$  min), (B) ACRN-1 ( $t = 20$  min), (C) ACRN-2 ( $t = 14$  min), and (D) ACRN-3 ( $t = 18$  min).

In Fig. 5A–D, we observed the characteristic peak at 400 nm gradually decreased and disappeared, and a new peak at about 310 nm gradually increased and red-shifted to 320 nm, indicating the generation of 4-aminophenol (4-AP). As we know, the work function of Ag was smaller than that of  $\text{Cu}_2\text{O}$ , so electrons were transferred from the  $\text{Cu}_2\text{O}$  shell to the Ag core. A large amount of positive charge was present on

the surface of  $\text{Cu}_2\text{O}$ , which attracted 4-NP to  $\text{Ag}@\text{Cu}_2\text{O}$  and accelerated the  $\text{BH}_4^-$  catalytic degradation, where the  $\text{BH}_4^-$  ions provided electrons for catalysis. Therefore, electrons moved from the depleted region near the  $\text{Ag}@\text{Cu}_2\text{O}$ -rGO interface to form an electron-rich region between  $\text{Ag}@\text{Cu}_2\text{O}$  and rGO. In the presence of rGO, these excess electrons promoted the absorption of electrons by the 4-NP molecules.

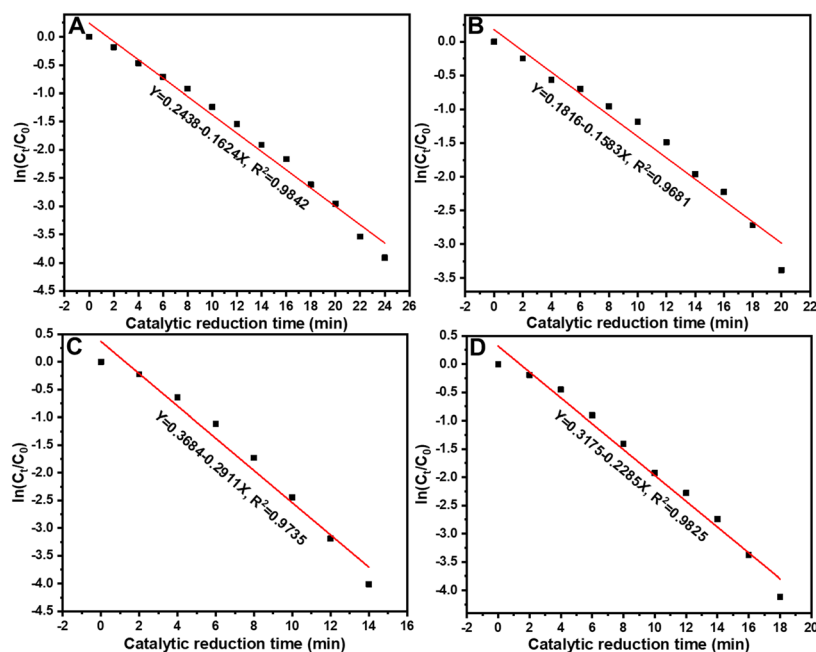


Fig. 6 Logarithm of  $C_t/C_0$  versus catalytic reduction time of (A) Ag-rGO and (B) ACRN-1, (C) ACRN-2, and (D) ACRN-3. The catalytic reaction rate constants for 4-NP are 0.16 (A), 0.16 (B), 0.29 (C), and 0.23  $\text{min}^{-1}$  (D).

By selecting rGO as the substrate for the composite, it could rapidly transfer carriers between the core-shell structure and also connect isolated core-shell particles in the surroundings. In addition, rGO had an efficient electron transfer platform, which could quickly transfer electrons, resulting in a high catalytic efficiency.

The ACRN exhibited porous structures and provided many active sites. During the catalytic reactions, the electrons on the Ag@Cu<sub>2</sub>O surface were transferred to BH<sub>4</sub><sup>-</sup>, and 4-NP was reduced to 4-AP. As shown in Fig. 5A–D, the complete degradation of 4-NP by Ag-rGO and three different ACRNs occurred in less than 24 min, indicating the excellent performance of the fabricated catalytic materials. Fig. 5C indicates that ACRN-2 exhibited the best catalytic efficiency, and the catalytic time was approximately 14 min. As shown in Fig. 6, the absorption logarithm  $[\ln(C_t/C_0)]$  and time ( $t$ ) exhibited a linear relationship, indicating that the catalytic reduction of 4-NP was related to the ACRN following a first-order kinetic relationship. The catalytic reaction rate constants for 4-NP were 0.16, 0.16, 0.29, and 0.23 min<sup>-1</sup>, indicating that ACRN-2 exhibited excellent catalytic activity, as the reaction rate was proportional to the reaction rate constant.

MO and TNP are abundantly present in soil and water, and the catalytic degradation of MO and TNP in water is necessary for environmental protection.<sup>31,32</sup> Therefore, the optimal ACRN-2 was utilized for the catalytic degradation of MO and TNP, which are toxic and explosive pollutants, and the catalytic process was observed by UV-vis absorption spectroscopy (Fig. 7A and B). The absorption peaks attributed to MO and TNP at 464 and 390 nm, respectively, gradually

decreased, indicating that MO and TNP were catalytically degraded, and ACRN-2 exhibited higher catalytic efficiency for MO than TNP. Furthermore, the linear relationship between the absorption logarithm  $[\ln(C_t/C_0)]$  and time ( $t$ ) in Fig. 7C and D indicated that the reduction process of MO and TNP was related to ACRN-2 and followed a first-order kinetic relationship. The catalytic reaction rate constants were 0.34 and 0.08 min<sup>-1</sup> for MO and TNP, respectively. The high absorption capacity of the ACRN is attributed to the abundant active sites on Cu<sub>2</sub>O. Meanwhile, the proposed study clearly demonstrated that the ACRN had excellent trace catalytic activity and high electron transfer efficiency, which resulted in excellent catalytic performance.

## Conclusions

To develop low-consumption and environmentally friendly organic pollutant degradation technologies, we designed an ACRN for the chemical reduction of potential pollutants. The morphology and properties of the ACRN were analyzed by UV-vis spectroscopy, TEM, and SEM. To study the catalytic activity of the ACRN, we selected 4-NP as a probe molecule and revealed the excellent chemical catalytic activity for the degradation of 4-NP. Notably, among the four catalytic materials with different Cu<sub>2</sub>O shell thicknesses, ACRN-2 exhibited excellent catalytic performance due to its superior electron transfer ability after the introduction of the rGO platform. More importantly, the fabricated ACRN exhibited excellent adsorption properties and significantly improved the degradation rate of 4-NP. In addition, the ACRN

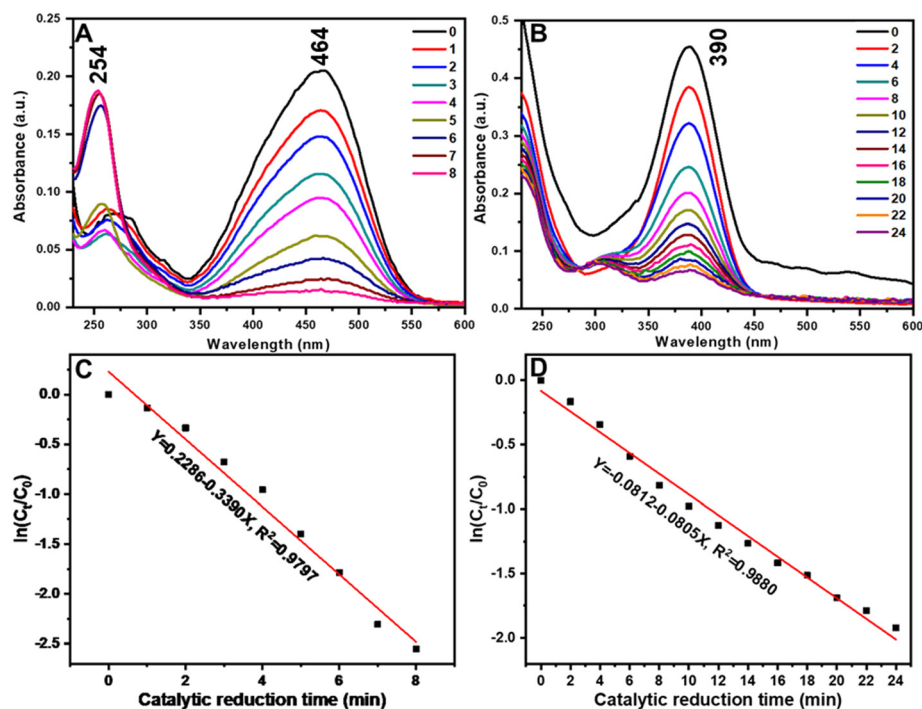


Fig. 7 UV-vis absorption spectra during the catalytic reduction of (A) MO and (B) TNP by introducing ACRN-2. Logarithm of  $C_t/C_0$  versus catalytic reduction time for (C) MO and (D) TNP. The catalytic reaction rate constants are 0.34 (C) and 0.08 min<sup>-1</sup> (D) for MO and TNP, respectively.

demonstrated the potential for the improvement for reduction of phenolic pollutants (MO and TNP). The catalytic reaction rate constants were 0.34 and 0.08 min<sup>-1</sup> for MO and TNP, respectively. This ACRN has significant potential for applications in catalytic systems for the removal of harmful substances from water. The use of graphene-based material in the catalytic study is of great significance for the development of nanomaterial science.

## Data availability

The datasets used and/or analyzed during the current study are available from the corresponding author on reasonable request.

## Author contributions

Lei Chen: methodology, data curation, formal analysis, and writing – original draft. Shuang Guo: data curation and formal analysis. Eungeong Park: investigation. Hongkai Zhao: methodology and funding acquisition. Young Mee Jung: conceptualization, writing – review & editing, supervision, and funding acquisition.

## Conflicts of interest

There are no conflicts to declare.

## Acknowledgements

This work was supported by the National Research Foundation of Korea (NRF) grants funded by the Korea government (RS-2023-00271205 and 2021R1A2C2004550) and by the Korea Basic Science Institute (National Research Facilities and Equipment Center) grant funded by the Ministry of Education (2020R1A6C101A195).

## Notes and references

- B. Lellis, C. Z. Fávoro-Polonio, J. A. Pamphile and J. C. Polonio, *Biotechnol. Res. Innov.*, 2019, **3**, 275–290.
- M. M. Hassan and C. M. Carr, *Chemosphere*, 2018, **209**, 201–219.
- A. Corma and P. Serna, *Science*, 2006, **313**, 332–334.
- M. S. Sekler, Y. Levi, B. Polyak, A. Novoa, P. S. M. Dunlop, J. A. Byrne and R. S. Marks, *J. Appl. Toxicol.*, 2004, **24**, 395–400.
- J. J. Song, Z. F. Huang, L. Pan, K. Li, X. W. Zhang, L. Wang and J. J. Zou, *Appl. Catal., B*, 2018, **227**, 386–408.
- G. Eichenbaum, M. Johnson, D. Kirkland, P. O'Neill, S. Stellar, J. Bielawne, R. DeWire, D. Areia, S. Bryant, S. Weiner, D. Desai-Krieger, P. Guzzie-Peck, D. C. Evans and A. Tonelli, *Regul. Toxicol. Pharmacol.*, 2009, **55**, 33–42.
- R. Liu, S. M. Mahurin, C. Li, R. R. Unocic, J. C. Idrobo, H. Gao, S. J. Pennycook and S. Dai, *Angew. Chem., Int. Ed.*, 2011, **50**, 6799–6802.
- M. Zhou, X. Wei, X. Zhang, X. Gao, X. Wang, W. D. Wu, C. Selomulya and Z. Wu, *J. Colloid Interface Sci.*, 2019, **537**, 112–122.
- I. Ghiat, A. Saadi, K. Bachari, N. J. Coville and A. Boudjemaa, *Res. Chem. Intermed.*, 2023, **49**, 4349–4365.
- S. C. Huang, Z. X. You, S. M. Jhang and C. Y. Lin, *J. Environ. Chem. Eng.*, 2022, **10**, 108882.
- P. Suchomel, L. Kvitek, R. Prucek, A. Panacek, A. Halder, S. Vajda and R. Zboril, *Sci. Rep.*, 2018, **8**, 4589.
- X. Chen, Z. Cai, X. Chen and M. Oyama, *J. Mater. Chem. A*, 2014, **2**, 5668–5674.
- M. Teimouri, F. Khosravi-Nejad, F. Attar, A. A. Saboury, I. Kostova, G. Benelli and M. Falahati, *J. Cleaner Prod.*, 2018, **184**, 740–753.
- L. Feng, G. Gao, P. Huang, K. Wang, X. Wang, T. Luo and C. Zhang, *Nano Biomed. Eng.*, 2010, **2**, 258–267.
- J. W. Gregory, Y. Gong, Y. Han, S. Huband, R. I. Walton, V. Hessel and E. V. Rebrov, *Catal. Today*, 2023, **418**, 114145.
- Z. Shang, Z. Yang, Y. Xiao and X. Wang, *Colloids Surf., A*, 2020, **604**, 125301.
- M. R. Shaik, S. F. Adil, M. Kuniyil, M. Sharif, A. Alwarthan, M. R. H. Siddiqui, M. I. Ali, M. N. Tahir and M. Khan, *Appl. Sci.*, 2020, **10**, 503.
- L. Chen, S. Guo, S. Di, E. Park, H. Zhao and Y. M. Jung, *Spectrochim. Acta, Part A*, 2024, **316**, 124354.
- F. Li, Y. Liu, T. Ma, D. Xu, X. Li and G. Gong, *New J. Chem.*, 2015, **39**, 6474–6481.
- L. Chen, M. Liu, Y. Zhao, Q. Kou, Y. Wang, Y. Liu, Y. Zhang, J. Yang and Y. M. Jung, *Appl. Surf. Sci.*, 2018, **435**, 72–78.
- L. Chen, S. Guo, L. Dong, F. Zhang, R. Gao, Y. Liu, Y. Wang and Y. Zhang, *Mater. Sci. Semicond. Process.*, 2019, **91**, 290–295.
- L. Xu, F. Zhang, X. Song, Z. Yin and Y. Bu, *J. Mater. Chem. A*, 2015, **3**, 5923–5933.
- K. S. Novoselov, A. K. Geim and S. V. Morozov, *Science*, 2004, **306**, 666–669.
- G. Yury, *Nat. Mater.*, 2015, **14**, 1079–1080.
- S. J. Guo and S. J. Dong, *Chem. Soc. Rev.*, 2011, **40**, 2644–2672.
- X. Huang, X. Y. Qi, F. Boey and H. Zhang, *Chem. Soc. Rev.*, 2012, **41**, 666–686.
- X. N. Chen, X. H. Wang and D. Fang, *Fullerenes, Nanotubes Carbon Nanostruct.*, 2020, **28**, 1048–1058.
- X. L. Deng, C. G. Wang, E. Zhou, J. Z. Huang, M. H. Shao, X. Q. Wei, X. J. Liu, M. Ding and X. J. Xu, *Nanoscale Res. Lett.*, 2016, **11**, 29–40.
- X. Xiong, L. Li, J. Chen, S. Zhang, L. Wang and S. Dou, *ACS Appl. Mater. Interfaces*, 2014, **6**, 15716–15725.
- S. Guo, Y. Wang, F. Zhang, R. Gao, M. Liu, L. Dong, Y. Liu, Y. Zhang and L. Chen, *Nanomaterials*, 2018, **8**, 444.
- Q. Lu, Z. Wei, C. Li, J. Ma and L. Li, *Mater. Sci. Semicond. Process.*, 2022, **138**, 106290.
- E. G. Kayser and N. E. Burlinson, *J. Energ. Mater.*, 1988, **6**, 45–71.